Proceedings of The ASME 2019
13th International Conference on Energy Sustainability
ES2019
July 15-17, 2019, Bellevue, WA, USA

ES2019-3898

ON-SUN CHARACTERIZATION OF MICROCHANNEL SUPERCRITICAL CARBON DIOXIDE SOLAR THERMAL RECEIVERS- PRELIMINARY FINDINGS

Erfan Rasouli, Caton W. Mande, Matthew M. Stevens
Western Cooling Efficiency Center
University of California, Davis, CA

Vinod Narayanan[1]
Western Cooling Efficiency Center and
Department of Mechanical and Aerospace Engineering
University of California, Davis, CA

ABSTRACT

The design of, and preliminary on-sun tests on, an 8 cm x 8 cm microchannel supercritical carbon dioxide (sCO_2) receiver is presented. The receiver has a laminated design, wherein sheets of Haynes 230 nickel superalloy are patterned and diffusion bonded to form microscale flow passages. The microscale pattern is in the form of square pins with width and height of 500 μm and 200 μm respectively. The pins are arranged in an in-line pattern with respect to the flow direction. The longitudinal and transverse pitch ratios of the micro pin fins are identical and equal to two times the side width of the pillar. A sCO_2 test facility is developed with the ability to supply sCO_2 at 200 bar pressure and at temperatures between 300-500°C to the receiver inlet. The sCO_2 facility is coupled to a seven meter diameter parabolic dish with a 25 kW rating and a concentration ratio of about 800. On-sun tests are performed at a receiver inlet pressure of 150 bar and a receiver inlet temperature between 110-130°C. Receiver and thermal efficiencies in excess of 0.91 and 0.96 respectively for the incident heat flux ranging from 8 to 80 W/cm^2, and average surface temperatures ranging from 150-550°C are obtained in these experiments.

Keywords: Concentrated Solar Thermal Power, Solar Thermal Receiver, Supercritical Carbon Dioxide Test Facility, Microchannel Solar Thermal Receiver, High Thermal Efficiency, High Temperature-High Pressure.

NOMENCLATURE

$A_{\min}$	Minimum flow area within the pin fin array (m^2)
A_{surf}	Surface area exposed to incident heat flux (m^2)
C	Solar concentration ratio
$D_{A\min}$	Hydraulic diameter calculated based on min $A_{\min}$ (m)
f	Friction factor
h_{amb}	Ambient natural convective heat transfer coefficient ($W / m^2 \cdot K$)
h_{in}	Enthalpy at the inlet of receiver (J / kg)
h_{out}	Enthalpy at the exit of receiver (J / kg)
I	Solar insolation (W / m^2)
$\dot{m}$	Mass flow rate (kg / s)
N_{row}	Number of longitudinal pin fin rows
ΔP	Pressure drop (Pa)
q_{fluid}	Absorbed heat by the working fluid (W)
$q_{incident}$	Incident heat onto the receiver surface (W)
$q''_{incident}$	Incoming incident heat flux onto the receiver surface (W / m^2)
$q_{loss,conv}$	Convection heat loss (W)
$q_{loss,rad}$	Radiation heat loss (W)
$q_{loss,refle}$	Reflection heat loss (W)
$\mathrm{Re}_{A\min}$	Reynolds number based on $D_{A\min}$
T_C	Heat rejection temperature (K)
T_{dish}	Solar dish surface temperature (K)
T_H	Heat addition temperature (K)
T_{in}	Receiver inlet temperature (K)

[1] Corresponding author.
Address: 2132 Bainer Hall, University of California Davis, Davis, CA 95616
E-mail address: vnarayanan@ucdavis.edu
Phone: (530) 752-9086
Fax: (530) 752-4158

T_{out} Receiver exit temperature (K)
T_{surf} Receiver surface temperature (K)
$V_{\max}$ Maximum velocity across pin fin array (m/s)

GREEK SYMBOLS
α_λ Absorptivity coefficient
ε_λ Emissivity coefficient
η_{rec} Receiver efficiency
$\eta_{theo\ rec}$ Theoretical receiver efficiency
$\eta_{theo\ rec,carnot}$ Theoretical Carnot solar cycle efficiency
η_{th} Thermal efficiency
μ Dynamic viscosity ($Pa.s$)
ρ Density (kg/m^3)
ρ_λ Reflectivity coefficient
σ Stefan-Boltzman constant ($W/m^2.K^4$)
τ_λ Transmissivity coefficient

SUBSCRIPTS
λ Function of wavelength
sCO_2 Supercritical carbon dioxide

INTRODUCTION

Solar thermal power plants that operate at high temperatures rely on the power tower design wherein heliostats concentrate the solar energy onto a receiver placed atop a central tower. In a typical power tower plant, the working fluid that is heated in the receiver exchanges heat with water in a heat exchanger (HX). The most common working fluid in the receiver (primary) loop is solar salt, a mixture of sodium and potassium nitrate. The steam generated in the HX goes through the Rankine cycle power block. The current status of molten salt technology, as represented by the Solar Two molten salt power plant, was assessed by Pacheco [1]. The Solar Two receiver was producing 565°C molten salt with a receiver efficiency of 88%, including an absorptivity of 95% and an average flux of 43 W/cm^2. In a more recent assessment, Kolb [2] estimated that next generation high temperature molten salt power towers could operate at fluxes up to 100 W/cm^2 with a corresponding thermal efficiency of 94% (excluding reflection losses).

In the past few years there have been several research efforts investigating the potential of supercritical carbon dioxide (sCO_2) for use as the working fluid in solar thermal plants. Advantages of using sCO_2 include smaller power block size, higher efficiency due to potential for higher exit temperatures in the receiver, and potential simplicity in power plant controls. Receiver design for such sCO_2 cycles is particularly challenging since the receiver efficiency must be higher than 90 percent at high fluid exit temperatures. From a structural standpoint, the receiver needs to be able to withstand surface temperatures of about 750°C and a pressure of about 200 bar.

There is limited open literature on sCO_2 solar receivers. Typical low-pressure gas-cooled central receivers have incident fluxes of 20 to 30 W/cm^2 [3].The US Department of Energy's Concentrating Solar Power program is funding the development of sCO_2 receivers among other technologies [4]. As a part of this program, Brayton Energy developed and characterized a heat-exchanger-style receiver with internal brazed fin architecture. A receiver thermal efficiency as high as 90.6% [4] was obtained with a creep lifetime of 90,000 hours. The National Renewable Energy Laboratory developed a cellular cavity sCO_2 receiver [4], in which absorber panels are arranged to form walls of repeating cellular cavity enclosures. Concentrated solar energy is partly absorbed and reflected on the walls of the panels within the enclosure. In lab-scale experiments a receiver efficiency as high as 94% at an outlet temperature of 650^{o}C and inlet temperature of 450^{o}C was obtained with a 3% reflective loss. A team of researchers at Oregon State University and University of California Davis have developed and characterized microchannel solar thermal receivers (MSTR) using simulations and lab-scale experiments on 2 cm x 2cm receivers [5-6]. Thermal efficiencies as high as 90% were achieved at incident heat flux of 68 W/cm^2 and an average receiver surface temperature of 720^{o}C. Thermal efficiency of 96.6% was achieved at a surface temperature of 650^{o}C and incident heat flux of 120 W/cm^2.

The use of a MSTR architecture for sCO_2 solar thermal cycles is further explored in this paper through the scaling up of a lab-scale receiver design and on-sun experiments. The goal of this paper is to present the design of an 8cm x 8cm MSTR architecture and characterize its performance with on-sun testing in a sCO_2 loop. Details of the facility and operational procedures are described as are the results of the on-sun test. The design constraints of the MSTR were based on DOE's Sunshot Concentrating Solar initial goals set in 2012 [7] with an operating pressure of 200 bar and an exit fluid temperature of 650^{o}C.

1. MSTR RECEIVER MODEL

It is envisioned that a scaled-up MSTR would consist of multiple unit cell panels. Each MSTR unit cell panel has its own inlet and exit ports that are in turn connected by appropriate manifolds to reduce down to two main pipes, which would carry the inlet and exit fluid streams. It is hence possible to characterize the performance of such an architecture by considering a single unit cell and developing appropriate headering. The efficiency of the MSTR unit cell is defined as the ratio of heat absorbed by the working fluid to that incident on the receiver surface,

$$\eta_{rec} = \frac{q_{fluid}}{q_{incident}} \quad (1)$$

where the rate of incident energy, $q_{incident}$, is obtained by an energy balance on the receiver,

$$q_{incident} = q_{loss,refle} + q_{fluid} + q_{loss,rad} + q_{loss,conv} \quad (2)$$

where the terms on the right side represent the surface reflection loss, heat transfer rate to the fluid, emission heat loss and heat loss to convection, respectively.

As a second receiver performance parameter, the thermal efficiency is defined as the ratio of the heat absorbed by the working fluid to the heat absorbed by the receiver,

$$\eta_{th} = \frac{q_{fluid}}{\alpha_{\lambda} \cdot q_{incident}} \quad (3)$$

where α is the surface absorptivity. Thus, in this efficiency definition, the reflection losses are not included. Therefore, the thermal efficiency is a measure of the efficacy of using microchannels without consideration of the performance of the optical coating on the receiver surface. The details of calculations of each parameter in Eqns. (1-3) are described in Section 4.

A simplified discretized model was developed to estimate the local bulk fluid temperature variation and the MSTR efficiencies. The length of MSTR was divided into a number of subsections with length of dx and a uniform incident heat flux, $q''_{incident}$, was assumed for each subsection. The internal flow heat transfer coefficient was determined using a correlation of flow across microscale pin fins developed by Rasouli et al. [8]. Details of the pin dimensions used for the model are described in the next section. The local surface temperature was used to determine the convective and emission losses. The surface reflectivity (ρ_{λ}) and emissivity (ε_{λ}) were assumed to be constant at 0.05 and 0.95, respectively. The sCO_2 inlet temperature and pressure was fixed at 500°C and 200 bar and the ambient temperature was set to 30°C.

Variation of receiver and thermal efficiencies for a 1m long x 1m wide MSTR is shown in Fig. 1 as a function of $q''_{incident}$ (Fig. 1a) and the sCO_2 exit temperature, T_{out} (Fig. 1b). Note that due to assumption of $\rho_{\lambda} = 0.05$ reflection heat loss is a constant ratio (5%) of the $q_{incident}$; hence thermal and receiver efficiencies follow a similar trend. In Fig. 1a, for a fixed system mass flow rate ($\dot{m}$) of 4.84 kg/s, an increase in $q''_{incident}$ results in an increase in receiver and thermal efficiencies. This is mainly due to smaller additional convection and radiation heat losses ($q_{loss,conv}$ and $q_{loss,rad}$) relative to the significant increase in the q_{fluid} . For example by increasing $q''_{incident}$ from 50 to 100 W/cm^2, the ratios of $q_{loss,conv} / q_{incident}$ decreased from 1.53% to 0.85% and $q_{loss,rad} / q_{incident}$ decreased from 4.82% to 3.10% respectively, while the $q_{fluid} / q_{incident}$ increased to 91.06% from 88.65%.

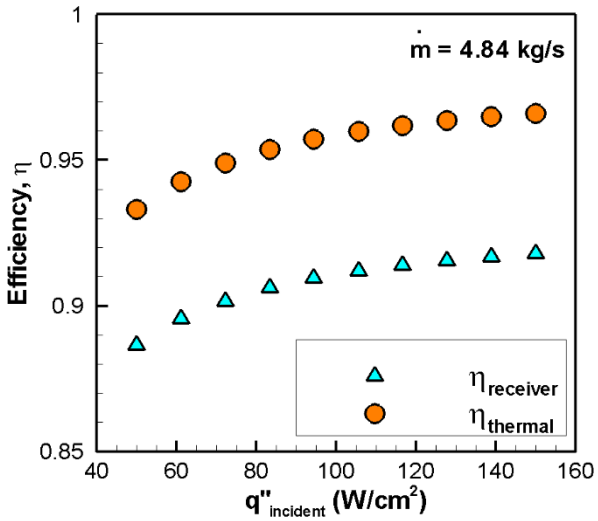

(a)

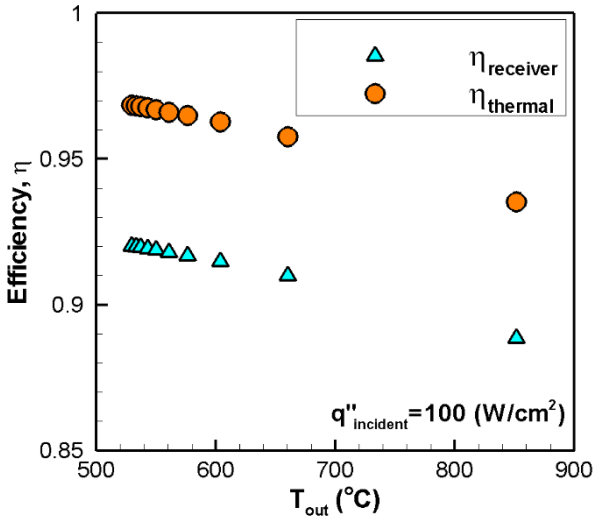

(b)

Figure 1. Variation of estimated receiver and thermal efficiencies with a) incident heat flux at fixed system mass flow rate and b) sCO_2 exit temperature at fixed incident heat flux.

The trend of efficiency as a function of outlet temperature is shown in Fig. 1b for a fixed inlet temperature and incident heat

flux $q''_{incident}$ of 100 W/cm^2. In contrast with Fig. 1a, it is seen that efficiencies decay with an increase in fluid outlet temperature T_{out}. Note that an increase in T_{out} corresponds to a decrease in system mass flow rate under fixed inlet temperature and incident heat flux. The T_{out} results in a higher receiver surface temperature (T_{surf}) and increased convective ($q_{loss,conv}$) and radiative emission ($q_{loss,rad}$) losses. At the same time, the lower flow rate at higher outlet temperatures results in decreased heat transferred to the fluid. These two aspects result in a decreasing efficiency trend observed in Fig. 1b.

Based on the model results presented in this section, it is clear that the MSTR is capable of a receiver efficiency in excess of 90% at a fluid exit temperature of 700°C and an incident heat flux of 100 W/cm^2. The rest of the manuscript describes the design of an 8cm x 8cm MSTR and its experimental characterization.

2. 8CM X 8CM MSTR DESIGN AND FABRICATION

An exploded view of the laminated 8cm x 8cm MSTR design is shown in Fig. 2a and the corresponding fluid volume is shown in Fig. 2b. Similar to the fabricated lab scale MSTRs in L'Estrange et al. [6], the 8 x 8 cm MSTR was fabricated from the nickel superalloy Haynes 230 using a combination of traditional mechanical machining and electric discharge machining. As shown in Fig. 2a, the MSTR is formed by diffusion bonding four laminae. The top two laminae have features that form fluid headers from inlet and exit piping to the microchannel pin array in the third lamina. The inlet stream is split between two unit cells each with an 8cm x 4cm plan area. Fluid is brought to the MSTR through a port located mid-way in the MSTR top lamina. From there, the fluid is routed to the ends and then into a plenum that spans the width of the MSTR in the second lamina. The fluid enters the micro-pin array located on the back side of the third lamina via slits on the top of the lamina. The slits were created using wire EDM while the micro pin array was machined using a slit cutter. The fourth layer at the bottom of the pin array encloses the micro pin fins to form the microscale flow passages. The micro pin fins were square with a width and height of 500µm and 200µm, respectively. The micro pin fins were arranged in an in-line pattern with respect to the flow direction and spaced with a pitch of 1000µm in both transverse and longitudinal directions. The thermofluidic parameters were set based on DOE's Sunshot goals [7], with an sCO_2 inlet temperature of 500°C, a system pressure of 200 bar, an sCO_2 exit temperature of 650°C and, a target incident heat flux of 100 W/cm^2. The design mass flow rate of 32 g/s was estimated based on the temperature receiver surface area, and incident flux.

The dimensions of the distribution headers were selected based on two criteria. First, to improve flow distribution into the pin finned flux plate (green layer in Fig. 2a), the pressure drop in the distributer headers needs to be significantly smaller than across the pin fin arrays. Second, the headers needed to be structurally designed to withstand the force of the 200 bar sCO_2. To address the latter, the side distributer headers were designed with ribs in order to reduce mechanical stress (see purple layer in Fig. 2a). A finite element analysis simulation was performed using ANSYS Mechanical on the side distributer header to ensure the maximum stress was below yield stress of Haynes 230 at the working fluid temperature. A computational fluid dynamics simulation using a commercial package, ANSYS Fluent, was then used to estimate the sCO_2 pressure drop in the headers for a nominal test flow rate of 32 g/s. The simulation showed pressure drop of about 14.5 kPa between the inlet into the side header and the farthest edge of the header.

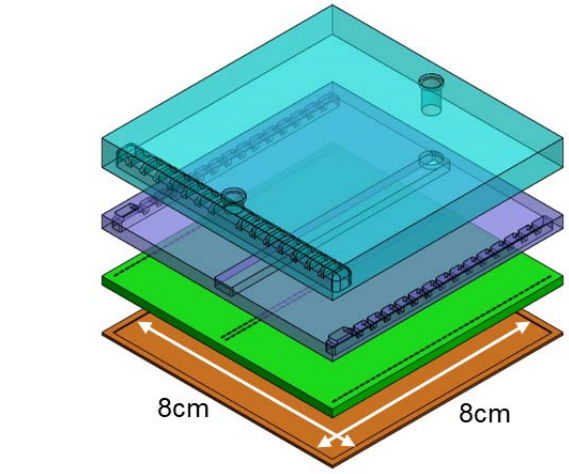

Figure 2. a) Exploded view of the finalized MSTR design and b) fluid passage in the 8cm x 8cm MSTR showing two unit cells in the flux plate

To ensure uniform flow distribution across the microchannel pin array, the pressure drop across the pin fin array should be significantly larger (~10 times) than the pressure drop across the distribution header. Either increasing the length of unit cell or decreasing the height of pin fins would help in increasing the pressure drop. An ANSYS Fluent simulation was performed to determine the appropriate dimensions for the unit cell. To reduce the computational time, a single row of pin fins was simulated from the inlet to exit section with periodic boundary conditions. For the 4cm wide unit cell (39.5mm fluid passage width) and 200µm pin fin height, the simulations showed approximately 176.5 kPa pressure drop at the design flow rate. This pressure drop was ~10 times larger than the pressure drop across the headers.

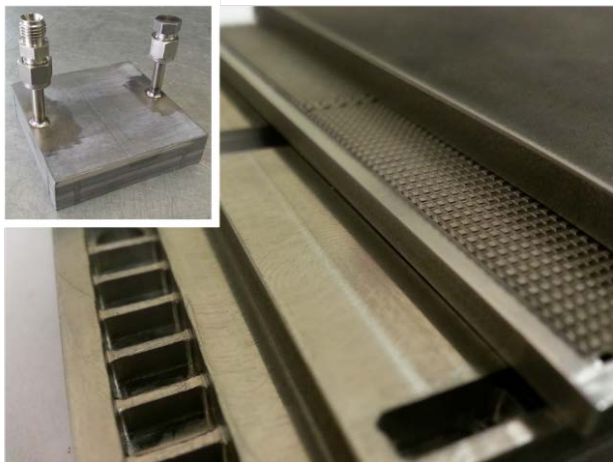

(a)

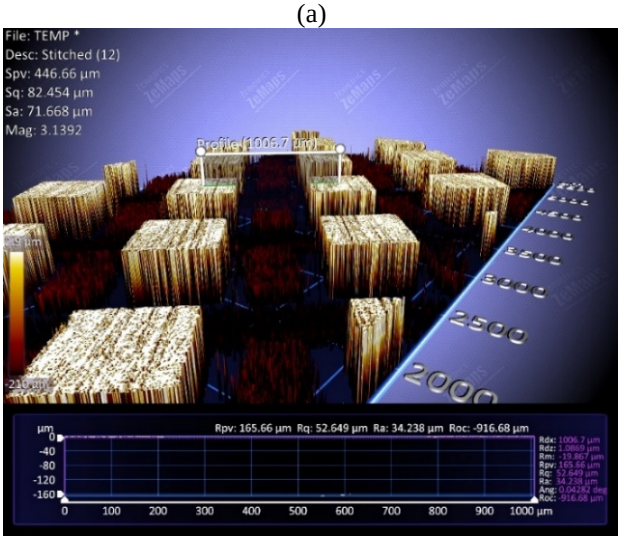

(b)

Figure 3. a) The laminates of the MSTR, inset picture shows the fabricated test section, b) surface profilametery from the flux plate showing the measured pitch distance (1007 µm) between two adjacent pin fins

Consequently, the final design for the subscale MSTR had 2 unit cells with 8cm length and4 cm width.

The laminae of the fabricated 8 cm x 8 cm MSTR are shown in Fig. 3a. Surface profilometery was performed on the fabricated plates to ensure the dimensions of the machined parts were in agreement with the design model. A Zygo 3D Surface Profiler was used to measure the pitch between two adjacent pin fins and is shown in Fig. 3b. As seen in Fig. 3b, the pitch was 0.6% different from the design value. The plates were electroplated with a nickel layer and then diffusion bonded. In order to provide an inlet and outlet to the test section, two quarter inch outside diameter (OD) Haynes 230 tubes were welded into the provided holes in the test section's header. A picture of the bonded MSTR is depicted in inset image in Fig. 3a. The fabricated MSTR was pressure tested at temperature to verify structural integrity and then tested on-sun. The facility used to perform these experiments is described in the following section.

3. TEST FACILITY DEVELOPMENT

3.1 MECHANICAL INTEGRITY TEST FACILITY

In order to test the mechanical integrity of MSTR at elevated temperatures, a pressure and temperature test facility was designed and built as shown in Fig. 4. The facility consisted of a 500,000 BTU/hr (165kW) burner that was connected to a test chamber using 21-inch circular galvanized steel ducting. The chamber was designed with 0.25" wall thickness steel plate with dimensions of 36" x 36" x 24" (height x width x depth). High temperature inorganic insulation lining covered the inner walls. The back and top walls were designed to be removable to permit the placement of, and access to the test article. High-pressure tubing and hydraulic hoses were used to connect the test article to an ultra-high pressure nitrogen cylinder (6000 psi) via an electronically-controlled pressure regulator and an electronically-controlled three-way diverting valve. The regulator was capable of adjusting the pressure from 1- 200 bar and was controlled by a LabVIEW program. The line pressure and the temperature of the thermocouples adhered to the test

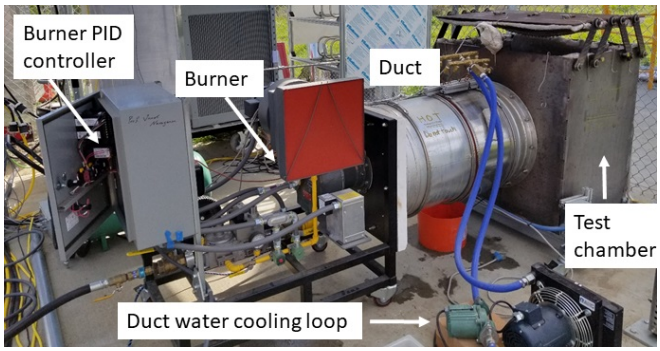

Figure 4. Phorograph of the pressure testing facility showing the chamber, duct, and burner

article were continuously recorded throughout the tests with the same LabVIEW program. The three-way diverting valve was used to isolate the test article from the cylinder upon application of pressure and during hold time. Furthermore, it was used to relieve pressure and re-pressurize the test article during cyclic pressure testing.

A PID controller on the burner was used to adjust the fuel-air ratio and hence the temperature. The temperature sensors for burner control were placed near the test article within the chamber. The intermediate duct was lined with a custom-made, refractory ceramic fiber insulation. To prevent overheating where the hottest part of the flame impinged on the insulation, an active cooling system was designed and installed on the outer diameter of the duct near the chamber. The cooling system utilized water-cooled copper coils wrapped around the duct and the heat was dissipated using a small air-cooled radiator. With this facility, test articles could be tested up to the desired operating temperature of 750°C.

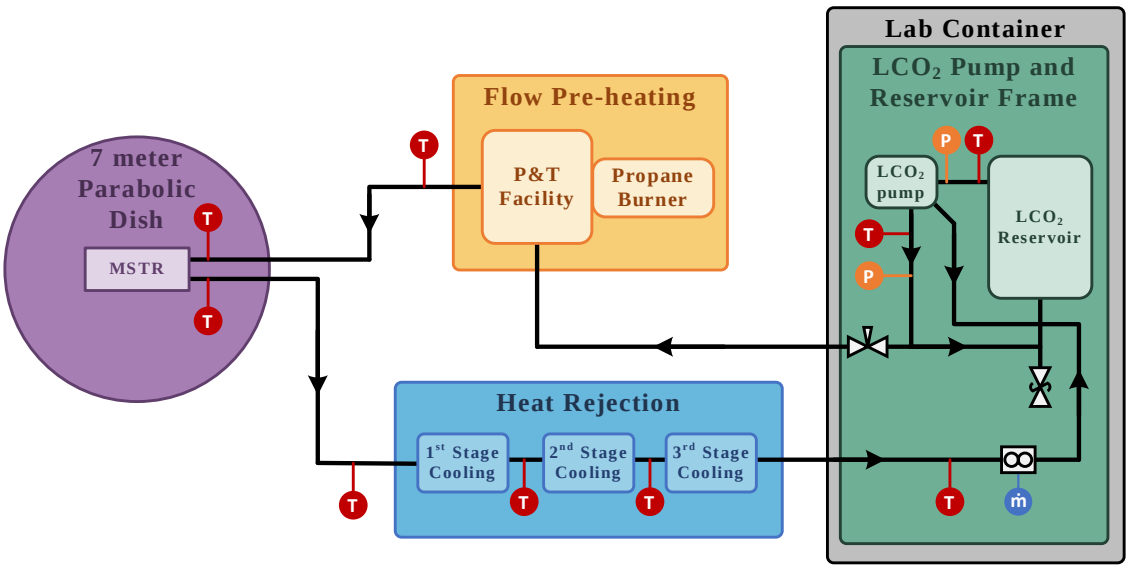

(a)

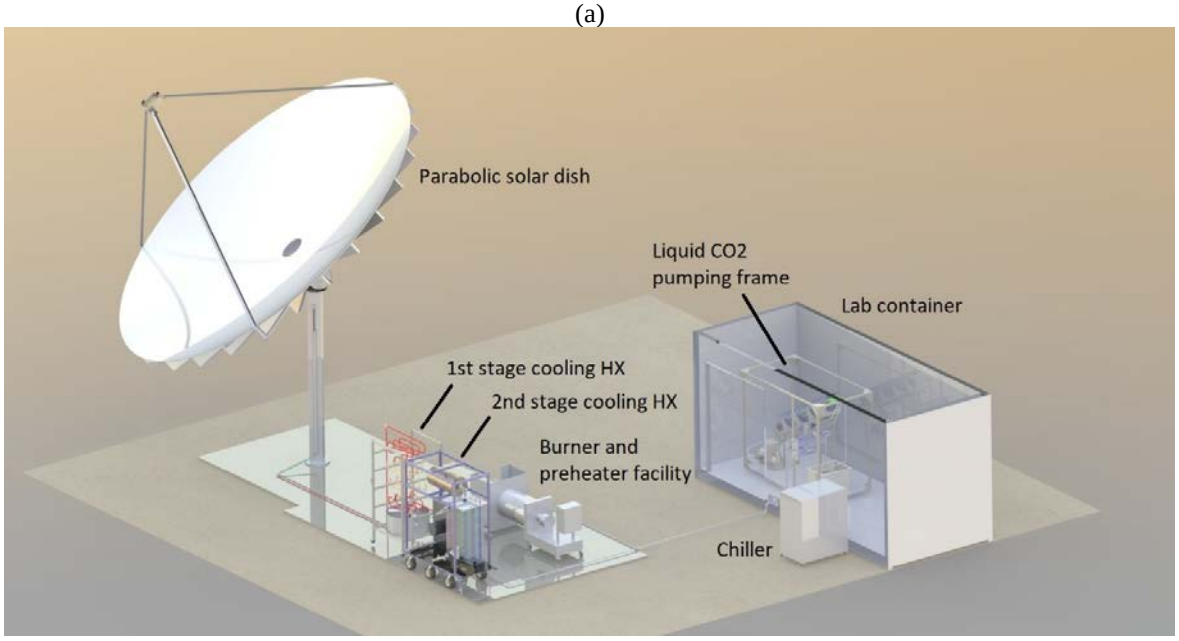

(b)

Figure 5. a) Simplified Schematic of the loop in operation b) 3D layout ot the solar site illustrating the component in relation with each other.

3.2 SOLAR-sCO_2 TEST FACILITY

A closed loop test facility was designed to supply high temperature and high pressure sCO_2 flow to the small scale MSTRs for on-sun testing. The loop was designed to accommodate testing MSTRs as large as 15cm x 15cm, absorbing heat fluxes up to 100 W/cm^2 into sCO_2 at 200 bar and with inlet and outlet temperatures of 550ºC and 720°C respectively. The loop consisted of four major sub-systems: 1) a pump and reservoir section, 2) a flow preheating section, 3) solar dish section, and 4) a heat rejection section. The aforementioned systems with annotations are depicted in Fig. 5a. The layout of solar site illustrating the position of the equipment in relation with each other is shown in Fig. 5b.

The charging system (not shown in Fig. 5a) consisted of a HPLC pump (Jasco PU-4088-CO_2) coupled to 850 psi CO_2 cylinders equipped with syphon tubes. The HPLC pump charges the reservoir and lines with liquid CO_2 (LCO_2) and raises the system pressure to the desired value. Prior to charging, a vacuum pump was used to evacuate the line in order to reduce the effect of contaminants and non-condensable gases. An electronically controlled three-way valve was located between the HPLC pump and the reservoir to permit switching operations between charging, closed loop operation, or release of CO_2 from the loop at the end of the experiment. The CO_2 was circulated through the loop using a two-stage high-pressure pump (Teikoku Chempump). The LCO_2 temperature and pressure was continuously monitored upstream and downstream of the pump, to prevent any cavitation within the pump housing. A high-pressure 7.5-gallon accumulator (without bladder) contained within a chilled water-glycol jacket was used as the LCO_2 reservoir. All of the equipment related to the charging and pumping sections were all installed on a rolling rack which was placed inside a modified shipping container (lab container), see Fig. 5b. A 5-ton air-cooled fluid chiller was used to provide chilled water-glycol solution to the LCO_2 reservoir cooling jacket, the HPLC pump, and the CO_2 condenser (discussed later in this section). In order to achieve efficient pumping performance, it was essential to keep the HPLC pump pistons chilled (≈5°C).

The pressure-temperature test facility described in Section 3.1 had a tubular heat exchanger installed in it to heat the LCO_2 to supercritical temperature before being sent to the MSTR. As seen in Fig. 5a and 5b, a 7m diameter parabolic dish (Solartron Energy Systems) was utilized for on-sun testing of the MSTRs. The dish is rated at a sun concentration ratio of 1000:1 and a thermal power of 25 kW at its focal point. The dish is equipped with two servo motors and can track the sun automatically and be remotely controlled. The sCO_2 is routed between equipment by 316 stainless steel tubing with a ¾ inch OD and a 0.12 inch wall thickness. The tube material and sizing were selected based on an operating pressure of 200 bar (at temperatures up to 720°C) and the lowest possible line pressure drop. Two seven-foot long, triple braided stainless steel hoses were used where the dish connects to its post to provide the flexibility required for sun tracking. The fluid lines along the dish arm to and from the focal point were bundled together. This was done so the sCO_2 could be further preheated by exchanging heat between the tubes to the inlet of MSTR. The burner heat input could be regulated based on the amount of heat exchange.

The outlet flow from the MSTR had to be cooled down to 21°C before being returned to the liquid CO_2 pump. Based on the designed system mass flow rate (105.4 g/s at 200 bar and 550°C), the total required heat rejection was 84 kW. A three-stage cooling process was used for heat rejection. In the first stage of cooling, the temperature was reduced to 250°C (39 kW cooling) using an air-cooled HX shown in Fig.5b. The total length of tubing used in the air-cooled HX design was 80 feet (24.4 m) and was bent to form a staggered bank of tubes within a plan area of 24in x 24in which was cooled by a 4500 cfm axially fan. In the second stage, an air-cooled radiator supplied water to a shell and tube HX to reduce the sCO_2 temperature down to ≈50°C (38 kW cooling). An aluminum box 18.5 inch x 22.5 inch x 46.25 inch served as HX shell and contained 120 feet (36.6 m) of tubing with 7 baffles spaced 12.7 cm from each other. Upon exiting the second cooling stage, the sCO_2 would return to the lab container and enter the third cooling stage. In the third cooling stage the sCO_2 was condensed back to LCO_2 at 21°C by passing through a 20ft (6m) coiled section of tubing immersed in a chilled water-glycol solution bath (rejecting about 7kW). As mentioned before, the chilled water-glycol was supplied by the 5-ton air-cooled fluid chiller. The condensed CO_2 was then directed through a Coriolis mass flow meter before returning back to the LCO_2 reservoir. Although the 8cm x 8cm MSTR was designed for 200 bar, the line pressure was restricted to 140 bar due to lower pressure rating of the Coriolis mass flow meter (~150 bar).

4. DATA REDUCTION AND UNCERTAINTY ANALYSIS

The key parameters of interest for on-sun characterization of the MSTR were the receiver and thermal efficiencies (Eqs. 1-3). In the following section, the methods used for quantifying the parameters which were shown in Eqns. (1-3) are discussed.

The absorbed heat by the working fluid (q_{fluid}) can obtained from,

$$q_{fluid} = \dot{m}\left(h_{out} - h_{in}\right) \tag{4}$$

where $\dot{m}$ refers to the mass flow rate of sCO_2, h_{in} and h_{out} are the inlet and exit sCO_2 enthalpy. The enthalpies were calculated at system absolute pressure and corresponding sCO_2 receiver temperatures, i.e. T_{in} and T_{out}. The incident heat rate ($q_{incident}$) in Eq. (1) can be determined using an energy balance represented in Eq. 2.

The reflected heat loss in Eq. (2) were obtained from a measure of the reflectivity of the flux surface, ρ,

$$q_{loss,refle} = \rho_\lambda \cdot q_{incident} \quad (5)$$

The radiation and convection heat losses from the surface of the receiver were obtained as:

$$q_{loss,rad} = \varepsilon \sigma A_{surf} \left(T_{surf}^4 - T_{dish}^4 \right) \quad (6)$$

and,

$$q_{loss,conv} = h_{amb} A_{surf} \left(T_{surf} - T_{amb} \right) \quad (7)$$

respectively, where T_{amb} is the ambient air temperature, T_{dish} is the dish surface temperature, T_{surf} is the receiver surface temperature, and h_{amb} is the convective heat transfer coefficient. The first two parameters were determined through temperature measurements of the air near the receiver and the back side of the parabolic dish. The surface temperature of the receiver varied by location on the receiver and was measured using an infrared camera. To calculate h_{amb} in Eq. (7), the empirical correlation for free convection from a tilted plate in Engineering Equation Solver (EES, F-Chart Inc.) was used.

The surface absorptivity, α_λ, in Eq. (3) for an opaque medium (no light transmission, $\tau_\lambda = 0$) can be found from,

$$\alpha_\lambda + \rho_\lambda = 1 \quad (8)$$

The surface emissivity coefficient, ε_λ, used in calculation of radiation heat loss, Eq. (6), also can be determined based on Kirchhoff's law of thermal radiation,

$$\varepsilon_\lambda = \alpha_\lambda \quad (9)$$

It was further assumed that the emissivity was equal to the absorptivity irrespective of wavelength (i.e. gray assumption). The microchannel receiver flux plate was painted with Pyromark® 2500 coating prior to on-sun testing. The reflectivity of the receiver flux plate was obtained by experimental measurements once the on sun testing was completed.

Based on the approach chosen to calculate the efficiencies, the following parameters needed to be measured during the on-sun experiments using the indicated instruments:

a. System absolute pressure, P (Absolute pressure transducer)
b. Microchannel receiver inlet and exit bulk fluid temperatures, T_{in} and T_{out} (K-type thermocouples)
c. Microchannel receiver surface temperature, T_{surf} (IR camera)
d. Ambient and dish surface temperatures, T_{amb} and T_{dish} (T-type thermocouples)
e. CO_2 fluid mass flow rate, $\dot{m}$ (Coriolis mass flow meter)

On-sun testing on 8cm x 8cm MSTR was performed over two days. For a steady state condition on test day 1, the representative bias errors in measured and determined variables are listed in Table 1. The Kline and McKlintock error propagation method [9] was used to determine uncertainties in the calculated parameters based on the bias errors of measured variables. Due to negligible precision errors at steady state conditions, only bias errors were incorporated in the uncertainty calculations. The uncertainties of thermocouples and absolute pressure transducers could be improved by calibration but it was found unnecessary because of large temperature difference between inlet and outlet of microchannel receiver.

Propagation of errors was performed using EES (Fchart Inc.). Maximum uncertainties in measured variables were propagated into the dependent variables using the aforementioned equations. The errors assume that the convection heat transfer coefficient correlation is accurate. Future work will be aimed at assessing the accuracy of the correlation and in the sensitivity of the prediction to uncertainty in efficiency.

Table 1. Representative measurement uncertainty estimate

Variable	Uncertainty (±)
sCO_2 temperature, K-type, T (°C)	Greater of ±1.1 or 0.4% reading
Surface/ambient, T-type, T (°C)	Greater of ±0.5 or 0.4% reading
sCO_2 absolute pressure, P_c (bar)	±0.88 (0.6%)
CO_2 mass flow rate, $\dot{m}_{sCO2}$ (g/s)	±0.1% reading
Surface reflectivity, ρ_λ	±3%
Absorbed heat by sCO_2, q_{fluid} (W)	±55.8 (4.5%)
Reflected heat from receiver, $q_{loss,refle}$ (W)	±3.6 (5.4%)
Heat loss due to radiation, $q_{loss,rad}$ (W)	±0.08 (0.6%)
Heat loss due to convection, $q_{loss,conv}$ (W)	±0.01 (1.2%)
Incident heat flux, $q''_{incident}$ (W/cm^2)	±0.92 (4.4%)
Receiver efficiency, η_{rec}	±0.00167 (0.18%)
Receiver thermal efficiency, η_{th}	±0.00086 (0.09%)

5. RESULTS

5.1 PRESSURE AND TEMPERATURE CYCLIC TESTING

The 8cm x 8cm MSTR shown in Fig. 6a was pressure tested up to 200 bar at temperatures up to 600ºC. The experiment consisted of three phases. First, the test article was pressure tested at ambient temperature. The pressure was ramped up from atmospheric to 200 bar (3000 psi) in ~35 bar intervals (500 psi) with a hold time of 5 minutes at each set pressure. In the second phase, the pressure was set to 200 bar and temperature increased up to 520 ºC. In the third phase, the test article temperature was

kept between 550-600 ºC and pressure was cycled between atmosphere and 200 bar with abrupt increase/decrease in pressure as shown in Fig. 6b. This cycle was repeated six times with a hold time of about two minutes. As seen in Fig. 6b, the receiver integrity at design pressure and temperature was verified.

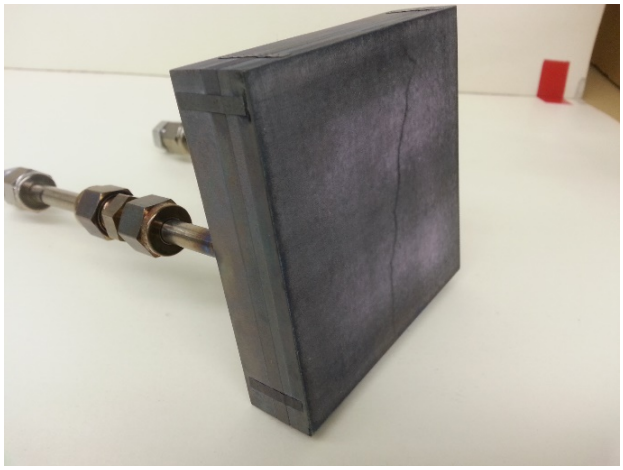

(a)

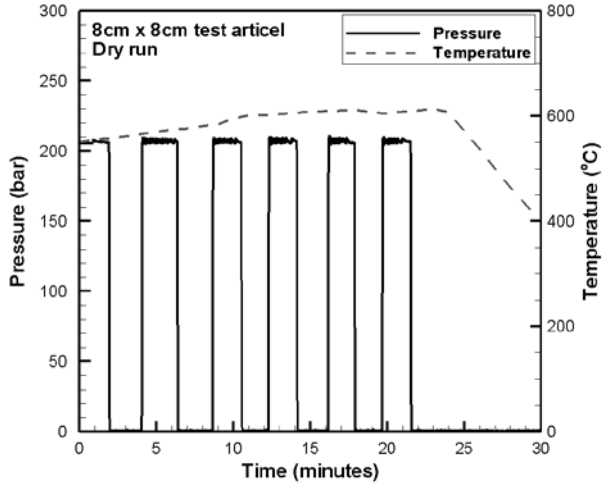

(b)

Figure 6. a) The 8cm x 8cm microchannel receiver used for dry run testing of P&T facility, b) P&T test results on 8cm x 8cm test article, pressure cycled at elevated temperature

5.2 FLOW DISTRIBUTION TESTING

The next step prior to placing the test article at the focal point of the dish, was performing a flow visualization test. The test article was placed at the exit of burner and preheated sCO_2 was run into the receiver (see Fig. 7a). The transient temperature contour map in the 8cm x 8cm MSTR is shown in Fig. 7b. As described in Section 3, the MSTR had two inlet headers and one exit header. The white arrows in Fig. 7b show the flow direction in the test article. Flow entering the receiver on the center left was split in two halves and were directed through headers on the very top and bottom. The flow then entered the microscale pin fin regions from these horizontal headers. The exit header-channel was located at the centerline of the microchannel where flow from both top and bottom microscale pin regions was collected. The exit header-channel extended to the very right where the exit tube guided the flow out of the receiver. For the flow distribution test, the system pressure was about 100 bar and the mass flow rate was varied from 15 to 33 g/s. The burner exit temperature was varied in the range of 145-550 °C. The receiver sides and back surfaces were insulated. The front of the receiver was exposed to air and imaged using an infrared camera.

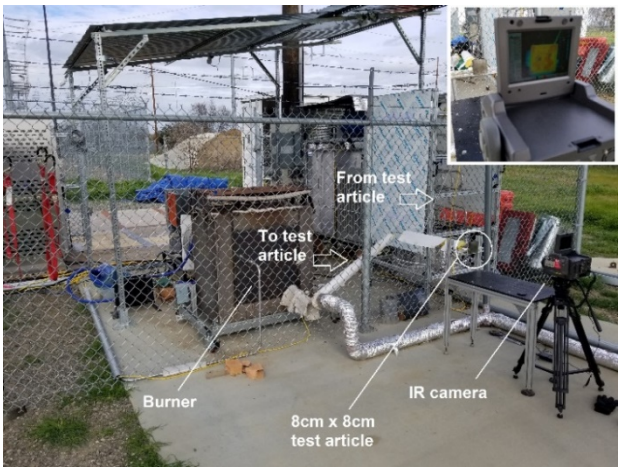

(a)

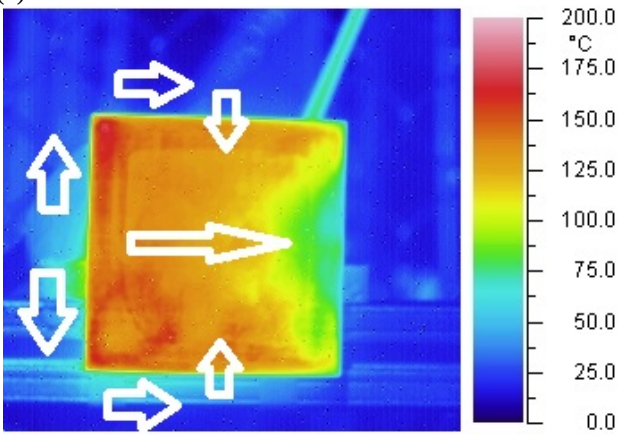

(b)

Figure 7. a) View of sCO_2 test facility configuration while running flow visualization experiment b) IR image from the flux surface of 8cm x 8cm test article revealing the temperature contours in transient condition.

As seen in Fig. 7b, the hot incoming flow first entered the region closer to the left where inlet tube was located which resulted in a more uniform temperature in that region. It was observed that 2/3rd of the 8cm x 8cm MSTR flux surface was quickly responsive to the temperature change at the exit of

burner while the temperature change of region closer to the exit tube lagged. It is clear from the transient image in Fig. 7b that the flow distribution was not uniform in the right side of the pin array. However, after about 2 minutes the whole flux surface would reach to a uniform temperature distribution. This uniformity could be attributed to conduction through the metal from hot region. Since the intent of using 8 cm x 8 cm MSTR was to verify the functionality of all the components in the solar-sCO_2 facility, on-sun experiments were performed despite the observed non-uniformity of flow. However, the process outlined in this section demonstrates the efficacy of the proposed flow distribution verification method.

5.3 PRESSURE DROP TESTING

To quantify the pressure drop through the 8 cm x 8 cm MSTR, the sCO_2 facility was modified to bypass the preheater, solar dish, as well as the 1st and 2nd cooling stages. The MSTR was mounted next to the CO_2 pumping frame shown in Fig. 5b. Two absolute pressure transducers and two K-type thermocouple were positioned at the inlet and exit ports of MSTR and data was collected under adiabatic conditions for the range of CO_2 mass flow rates. The inlet CO_2 pressure varied from 125-139 bar for the collected steady states points. The variation of non-dimensional pressure drop (friction factor) as a function of the Reynolds number is shown in Fig. 8a. The friction factor, f, and Reynolds number were obtained from:

$$\mathrm{f} = \frac{\Delta P}{N_{row} \times \frac{1}{2}\rho V_{\max}^{\ 2}} \tag{10}$$

and

$$\mathrm{Re}_{A\min} = \frac{\rho V_{\max} D_{A\min}}{\mu} \tag{11}$$

respectively, where N_{row} is the number of longitudinal pin fin rows through which the flow traverses from inlet and outlet plena, and $V_{\max}$ is the maximum velocity that flow experiences when passing through the pin fin array's minimum transverse flow area ($A_{\min}$). The density and dynamic viscosity of CO_2, ρ and μ, were calculated at the average temperature and pressure between inlet and outlet ports. From Eq. (11), it can be seen that Re is calculated based on a hydraulic diameter obtained at $A_{\min}$ and not based on an individual micro pin fin as per the definition in prior work by the group; the readers are referred to Rasouli et al. [8] for further discussion regarding the selection of appropriate length scale in micro pin fin arrays. As seen in Fig. 8a, the CO_2 friction factor decays with increasing $\mathrm{Re}_{A\min}$.

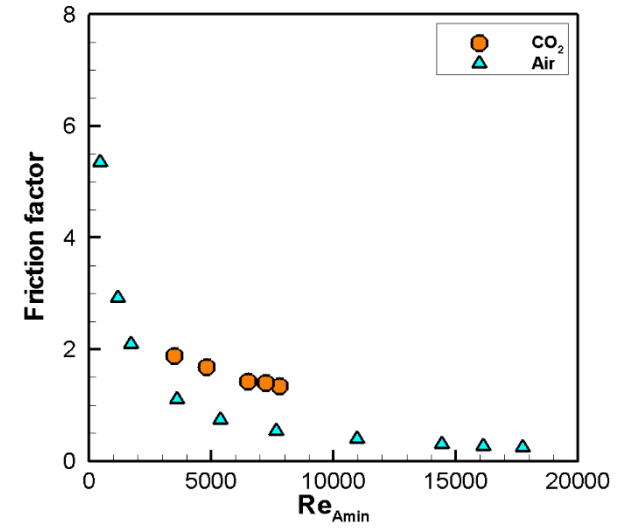

(a)

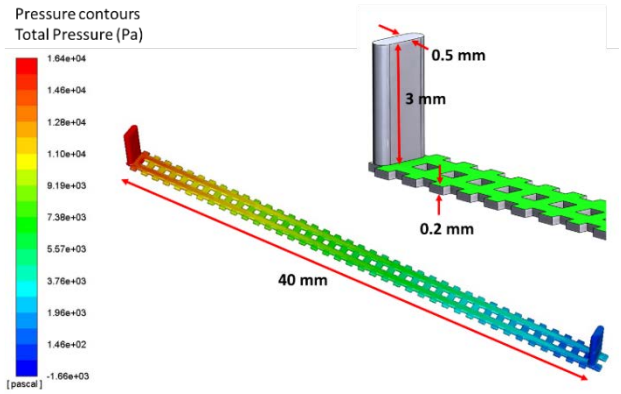

(b)

Figure 8. a) Variation of friction factor with Re number of CO_2 and air flow in the 8cm x 8cm MSTR, b) the pressure contours map in a MSTR sectioned model.

The pressure drop corresponding to the plotted f varied from 1.4 bar to 6.8 bar for $3500 < \mathrm{Re}_{A\min} < 7800$. Due to significantly high measured pressure drop, CFD simulation was performed at the similar flow conditions. As discussed in MSTR design process (Section 3), a single row of 40 pins from inlet to exit with lateral periodic boundary conditions was simulated as shown in the inset picture of Fig. 8b. Simulation was performed using the shear stress transient two equation eddy-viscosity turbulence model with $k-\omega$ model using an equivalent mass flow rate with the assumption of uniform flow distribution between the two unit cell arrays and in the lateral direction. The predicted pressure drop was significantly lower than in the experiments. For example at $\mathrm{Re}_{A\min} = 7800$, the experimental pressure drop was 6.8 bar (680kPa) where the CFD simulation showed only 0.1612 bar (16.12 kPa). It should be noted that the simulation did not cover the pressure drop along the distribution

header and welded tubing on top of the inlet/outlet ports. However, considering the header dimensions, the largest pressure drop was expected across the pin fin array.

Fig. 8a includes the pressure drop of air flow through the 8cm x 8cm MSTR performed in a different test apparatus. It can be seen that for a given Re number, the friction factor in air flow is smaller than that of CO_2 flow. For example at $Re_{Amin} = 7650$, the air pressure drop was 4.9 bar, compared with 6.8 bar in CO_2 flow at $Re_{Amin} = 7800$ (28% smaller). Running the CFD simulation for this case showed 0.191 bar (19.1 kPa) which again is significantly below the experimental pressure drop within MSTR. The internal channels of MSTR need to be further examined either non-intrusively via Neutron Radiography/X-Ray tomography or by section cutting to measure the channel dimensions. There is a chance for excess strains on the micro pin fins during diffusion bonding of the laminae, which could result in smaller channel dimensions than the design values. Additionally, the impact of surface roughness using the mechanical slit cutters (Ra = 34 μm, see Fig. 3b), which was 20% of the pin height, on pressure drop needs to be investigated.

5.4 ON-SUN TESTING

The 8cm x 8cm MSTR was installed at the focal point of the dish. High temperature ceramic fiber board (Duraboard®) was placed around the microchannel receiver to eliminate incoming heat flux from the test article surroundings and protect the temperature sensors. The loop was charged with CO_2 prior to the test day. The test was started by turning on the liquid CO_2 pump to circulate the flow through the lines while the dish was in stow-away position. Subsequently, the CO_2 preheater was fired up to provide sCO_2 at temperature range of 85-90 °C at the inlet to the receiver. Once the temperature, pressure and flow rate readings became stable over a period of 15 minutes, dish tracking was enabled. Figures 9 shows pictures of the dish and receiver area during the first day of testing. Some wispy white cloud cover was observed visually during the duration of the test; the cloud cover increased with progression of the test.

A time series of fluidic conditions at the commencement of tracking is shown in Figure 10. Comparing the receiver inlet and outlet temperatures, it can be seen that the receiver exit temperature rapidly increased from ~85°C to above 160°C. It can be seen that the receiver inlet temperature followed a gradually increasing trend upon tracking the sun (see minute ~16 in Fig. 10) and plateaued after about 25 minutes. This increase was at least in part attributed to heat exchange between the inlet and exit flows to/from the receiver. The tubes were strapped together all along the solar dish post and arm in order to recuperate part of the absorbed heat by the receiver for preheating the inlet stream. Additionally, there might have been an increase in inlet temperature due to heat conduction from the mass of the hot receiver metal to the thermocouple location. During this transient, the system mass flow rate experienced a slight decrease, from 22.1 g/s to 20.5 g/s (see Fig. 10) while the system pressure increased slightly from 142.5 bar to 149.5 bar. Note that the mass flow rate was only 64 percent of the design flow rate; higher flow rate could not be achieved due to the pressure drop across the Coriolis mass flow meter used in the experiment. For a given system pressure, the sCO_2 density is inversely related to temperature; the higher the temperature, the lower the density. For a given temperature, density would vary directly with pressure.

(a)

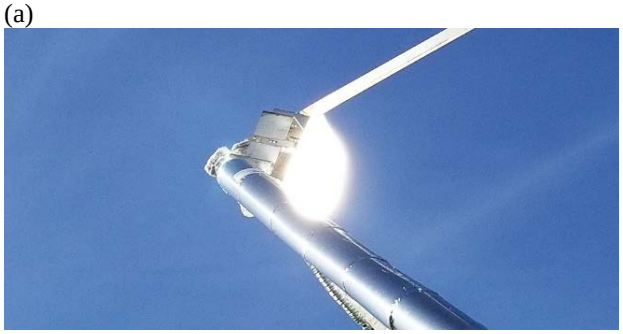

(b)

Figure 9. Test day 1. a) The solar dish while tracking the sun and heating up the sCO_2 flow across the microchannel receiver b) close-up view from the solar dish focal point where the black painted 8cm x 8cm test article cannot be distinguished from the surrounding insulation due to the concentration.

The combination of the increased temperature and pressure during the transient resulted in a slight decrease in mass flow rate. It is worth mentioning that the CO_2 temperature in the fluidic lines after 2nd stage cooling and within the CO_2 pumping frame were unchanged before and after start of tracking, indicating that the cooling stages were able to manage the load generated by the preheater and the receiver.

Since the first day of testing occurred during the latter hours of the day and solar insolation was relatively low, the experiment was repeated the following day to obtain higher heat flux data. Similar to the first day, the time series for a truncated period of time before and after start of sun tracking is shown in Fig. 11a. The start time of the time series corresponds to 11:55 AM of March 7th, 2018. The conditions were intermittently sunny with some cloud cover; see Fig. 11b. The solar radiation based on the local weather station report varied about 470-510 W/m^2 (higher than previous day) and even reached to 700 W/m^2 closer to 3:00 PM.

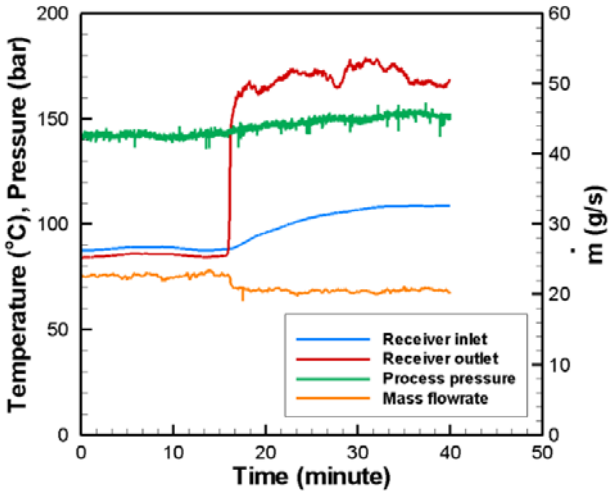

Figure 10. Test day 1. Time series of the temperature, pressure, and mass flow rate sensors' readings for the period of time before and after start of sun tracking. Start time was at 3:43 PM on March 6th, 2018.

The sensors' readings generally followed the same trends as they did in test day 1 with some differences. It can be seen that due to existence of bulky and patchy clouds the jump in the microchannel receiver exit temperature occurred in several steps, starting first with $\Delta T = 42.5°C$ (at t=3-4 minutes in Fig. 11a) and it reached to $\Delta T = 176.2°C$ (at t=21 minutes in Fig. 11a) where ΔT is the sCO_2 temperature difference between exit and inlet of MSTR. This pattern is different from what was observed in test day 1, compare Fig. 11a with Fig. 10. In test day 1, the clouds were not patchy and the cloud strands stretched and covered the entire horizon which is why the exit temperature didn't fluctuate significantly. The steady state mass flow rate before sun tracking was ~27 g/s and it decreased to 19.7 g/s (at t > 17 minutes). The significant drop in flow rate in day 2 tests compared with day 1 could be attributed to the substantially larger variation in temperature in day 2. As seen in Fig. 11a at t=15 minutes in contrast with system pressure-temperature relation discussed earlier, there is a slight decrease in the pressure while the exit temperature increases. This decrease was caused due to an intentional purge of CO_2 downstream of the 2nd cooling stage to keep within the pressure limit of the Coriolis mass flowmeter of 150 bar.

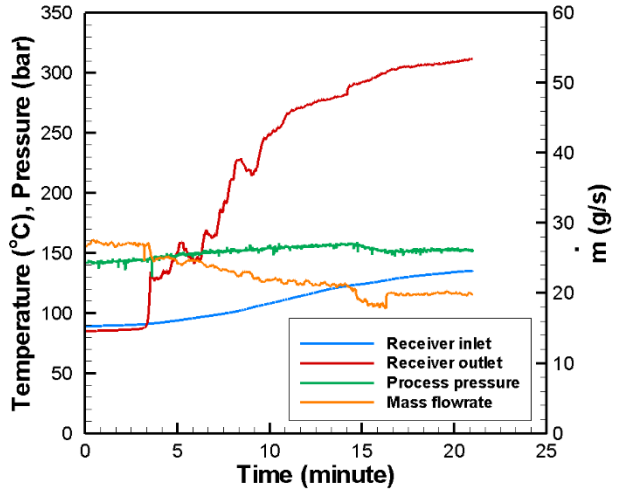

(a)

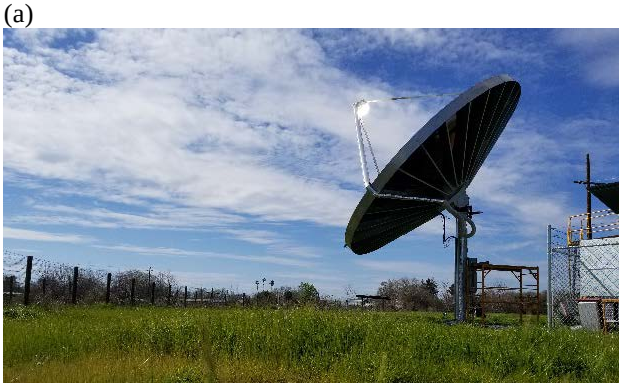

(b)

Figure 11. a) Test day 2. Time series of the temperature, pressure, and mass flow rate sensors' readings for the period of time before and after start of sun tracking. Start time 11:55 AM on March 7th, 2018. Solar insolation ranged from 470-510 W/m^2.

5.5 MSTR EFFICIENCIES

Sensors' readings were recorded at 2 Hz frequency. The recorded data was analyzed and a number of time periods were extracted in which the sensors' readings were relatively steady. For example, in the extracted 30-second intervals the T_{out} varied less than 0.9°C. The readings were averaged over the interval duration and were analyzed using the equations discussed in the Data Reduction section to calculate the desired parameters, i.e. receiver efficiencies.

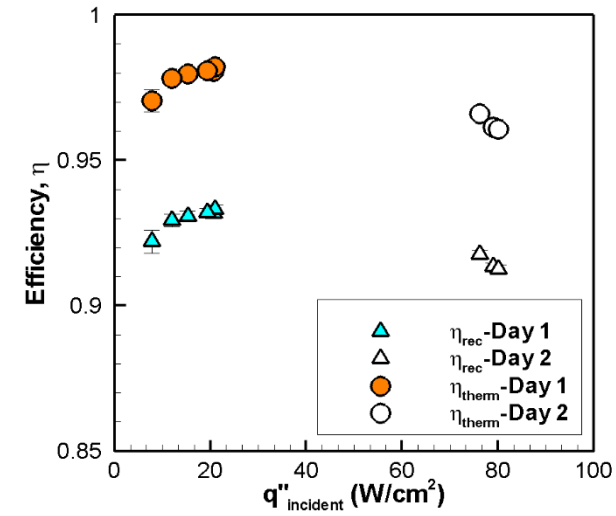

(a)

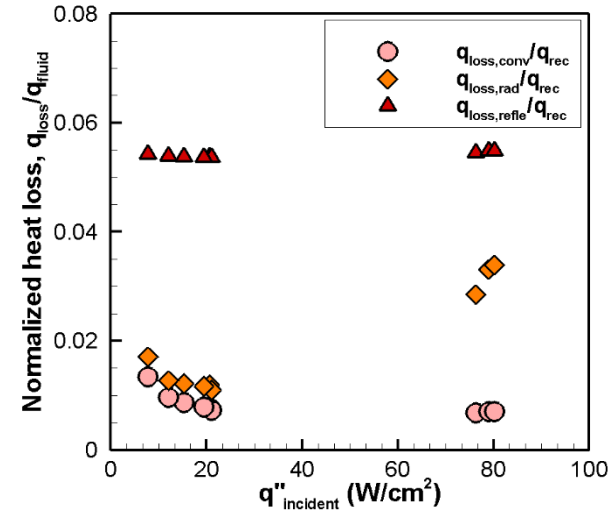

(b)

Figure 12. a) Variation of receiver efficiency and receiver thermal efficiency with incident heat flux in both test days, b) The trend of heat losses normalized by q_{fluid} as a function of $q''_{incident}$. T_{surf} varied in the range of 142-199°C and 510-554°C respectively for data related to test days 1 and 2.

The variation of receiver efficiency and receiver thermal efficiency as a function of incident heat flux for both test days are shown in Fig. 12a. The incident heat flux, as calculated using Eq. (2), ranged from 8-21 W/cm^2 and 76-80 W/cm^2 on test days 1 and 2 respectively. Limited open literature exists on sCO_2 solar receivers. Typical gas-cooled central receivers have incident fluxes in the range of 20 to 30 W/cm^2 [3]. For the range of $q''_{incident}$, it can be seen in Fig. 12a that both thermal and receiver efficiencies were greater than 0.90. The maximum values for η_{rec} and η_{th} are respectively 0.93 and 0.98 for $q''_{incident}$ of 21 W/cm^2. It can be seen that at higher $q''_{incident}$ there is a slight decrease in the efficiencies. This can be better understood by looking at the trends of individual heat loss components' at higher $q''_{incident}$. The three involved heat losses which were identified in Eq. (2) were calculated and normalized by q_{fluid} and are plotted as a function of incident heat flux, $q''_{incident}$, in Fig. 12b so they can be compared with corresponding η values shown in Fig. 12a. Comparing the ratios (q_{loss}/q_{fluid}) in low and high $q''_{incident}$ in Fig. 12b, it can be seen that reflection and convection loss ratios are approximately unchanged. However, the radiation loss ratio significantly increases at higher incident heat fluxes. This is mainly due to higher surface temperatures on day 2 of testing with a T_{surf} of 510°C-554°C compared to a T_{surf} of 142°C-199°C on day 1. Although $q_{loss,rad}$ was identified as the main reason behind changes in η values at different $q''_{incident}$ it should be noted that at any tested $q''_{incident}$, the ratio of $q_{loss,refle}/q_{fluid}$ is the greatest of all heat loss components. Hence the black coating or any technique in surface treatment in order to minimize surface reflectivity, ρ, seems crucial in increasing the microchannel receiver efficiency, η_{rec}.

5.6 MICROCHANNEL RECEIVER FAILURE

In the middle of test day 2 while the solar dish was tracking the sun, a hissing sound emanated from the loop in the area of the 8cm x 8cm receiver. Emergency shut down procedures developed as part of sCO_2 test facility operation were followed to safely and successfully terminate the experiment and diagnose the issue. The shutdown procedure included a) moving the dish from an on-sun to stow-away position, b) turning off the preheater burner, c) shutting down the liquid CO_2 pump, and d) isolating the CO_2 pumping station which contains the liquid CO_2 reservoir from the rest of fluidic lines. Once the remaining CO_2 in the lines connected to the microchannel receiver was drained, the solar dish was turned toward the receiver installation station so the operator could investigate the cause for the leak. An immediate visual inspection revealed that the leak was due to a pinhole failure on the lower side of the receiver, see Fig. 13a. It is also clear that the Pyromark® 2500 coating didn't hold its integrity and peeled off at several locations. The coating integrity could be improved by following rigorous heat treatment procedures [10]. The IR pictures of transient temperature distribution like the one shown in Fig. 7b implied the existence of flow mal-distribution. Figure 13b shows the IR picture taken from 8cm x 8cm test article during flow distribution visualization, but rotated to match the orientation of the installed receiver on the solar dish. The cold spot (circled green-blue

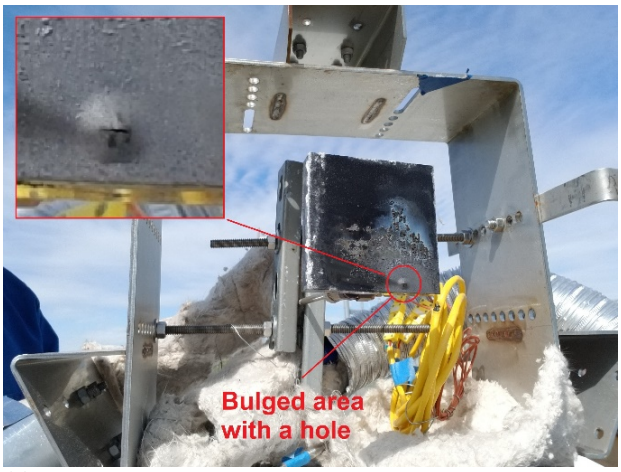

(a)

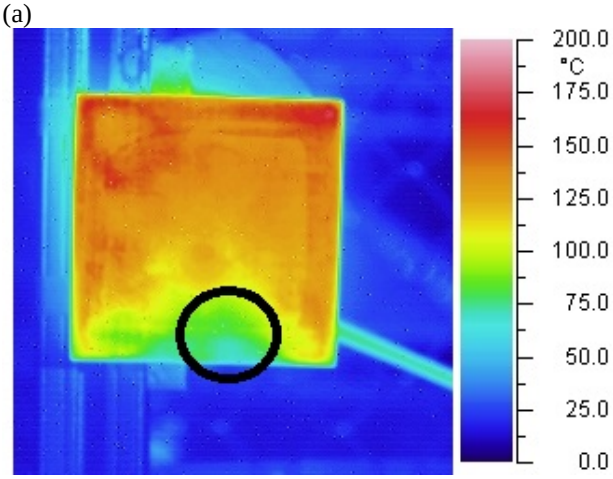

(b)

Figure 13. a) Picture of the microchannel receiver right after failure showing the bulged region, b) IR image of the microchannel receiver during flow visualization testing.

region) shown in Fig. 13b corresponded to the area where heated sCO_2 was likely not flowing. This marked region corresponded closely with the rupture location shown in Fig. 13a. Further investigation is underway to determine the cause for the mal-distribution through neutron and x-ray radiography and microscopy.

6. CONCLUSIONS

A microchannel solar thermal receiver was designed, fabricated and tested on-sun in a solar-sCO_2 loop. The MSTR was fabricated by diffusion bonding of 4 laminae out of Haynes 230. The MSTR was successfully pressure tested at temperature and was installed on the focal point of a 7m diameter solar dish. The solar-sCO_2 facility developed for on-sun test was capable of supplying sCO_2 at elevated temperatures with mass flow rate and pressure up to 105 g/s and 200 bar, respectively. The findings of the study can be summarized as:

- A laminated MSTR with microscale pin fins with a foot print of 8cm x 8cm made by use of wire EDM on Haynes 230 could be successfully diffusion bonded- leak free.
- The MSTR passed the following mechanical integrity tests: 200 bar pressure at ambient temperature, 200 bar pressure at 520°C, and cyclic pressure testing between 1-200 bar at elevated temperatures up to 600°C.
- Flow distribution visualization and pressure drop experiments revealed some drawbacks in the design which necessitate further studies in design of headers and in the fabrication process.
- After initiation of sun tracking, it was observed that the system operating pressure and mass flow rate undergoes noticeable transients (increase in pressure and decrease in the mass flow rate) suggesting that further system startup and shutdown considerations are warranted.
- The MSTR could absorb heat fluxes in the range of 8-80 W/cm^2 with both thermal and receiver efficiencies greater than 0.91. The maximum values for η_{rec} and η_{th} were respectively 0.93 and 0.98 at T_{surf} of 192.5 °C (corresponding to $q''_{incident}$ of 21 W/cm^2).

Further improvements to the test facility to permit higher inlet temperatures to the receiver are underway. Additionally, further design improvements are being made by partner institutions in the project.

ACKNOWLEDGEMENTS

Financial support by DOE EERE grants # DE-EE0005801 and DE-EE0007108 is gratefully acknowledged. The authors would like to acknowledge the contribution of their colleagues, Drs. Kevin Drost, Sourabh Apte, Brian Fronk, and Thomas L'Estrange at Oregon State University.

REFERENCES

[1] Pacheco, J.E., 2002. Final test and evaluation results from solar two project. In: Sandia National Laboratory, Albuquerque, NM, p. SAND2002-0120.

[2] Kolb, G.J., 2011. An evaluation of the next generation of high temperature molten salt power towers. In: Sandia National Laboratory, Albuquerque, NM, p. SAND11-9320.

[3] Romero, M., Buck, R., Pacheco, J.E., 2002. An update on solar central receiver systems, projects, and technologies. Journal of Solar Energy Engineering, 124, pp. 98-108. http://dx.doi.org/10.1115/1.1467921.

[4] Mehos, M., Turchi, C., Vidal, J., Wagner, M., Ma, Z., Ho, C., Kolb, W., Andraka, C., Kruizenga, A., 2017, Concentrating Solar Power Gen3 Demonstration Roadmap, Technical Report NREL/TP-5500-67464.

[5] Narayanan, V., Fronk, B. M., L'Estrange, T., and Rasouli, E., 2019, "Supercritical Carbon Dioxide Solar Thermal Power Generation- Overview of the Technology and Microchannel Receiver Development," Chapter 11, Advances in Solar Energy Research, Springer Nature series on Energy, Environment and Sustainability, Editors: H. Tyagi et al., https://doi.org/10.1007/978-981-13-3302-6_11

[6] L'Estrange, T., Truong, E., Rymal, C., Rasouli, E., Narayanan, V., Apte, S., Drost, K., 2015. High flux microscale solar thermal receiver for supercritical carbon dioxide cycles. In: ASME 2015 13th International Conference on Nanochannels, Microchannels, and Minichannels. ASME, San Francisco, CA, http://dx.doi.org/10.1115/ICNMM2015-48233.

[7] U.S. Department of Energy, 2012. High efficiency receivers for supercritical carbon dioxide cycles. In: SunShot Concentrating Solar Power Project Description, p. DOE/GO-102012-3661.

[8] Rasouli, E., Naderi, C., Narayanan, V., 2017, "Pitch and Aspect Ratios Effects on Single-Phase Heat Transfer through Microscale Pin Fin Heat Sinks", International Journal of Heat and Mass Transfer, Vol. 118, pp. 416-428, https://doi.org/10.1016/j.ijheatmasstransfer.2017.10.105

[9] Moffat, R., 1988. Describing the uncertainties in experimental results. Journal of Experimental Thermal and Fluid Science, 1 (1), pp. 3-17.

[10] L'Estrange, T., 2015, Experimental Characterization of a Supercritical Carbondioxide Microchannel Solar Thermal Receiver, M.S. Thesis, Oregon State University.